

Symbolic Pauli Propagation for Gradient-Enabled Pre-Training of Quantum Circuits

Saverio Monaco ,^{1,2} Jamal Slim ,² Florian Rehm ,³ Dirk Krücker ,² and Kerstin Borras ,^{1,2}

¹*RWTH Aachen University, Aachen 52062, Germany*

²*Deutsches Elektronen-Synchrotron DESY, 22603 Hamburg, Germany*

³*European Organization for Nuclear Research (CERN), Geneva 1211, Switzerland*

(Dated: December 22, 2025)

Quantum Machine Learning models typically require expensive on-chip training procedures and often lack efficient gradient estimation methods. By employing Pauli propagation, it is possible to derive a symbolic representation of observables as analytic functions of a circuit's parameters. Although the number of terms in such functional representations grows rapidly with circuit depth, suitable choices of ansatz and controlled truncations on Pauli weights and frequency components yield accurate yet tractable estimators of the target observables. With the right ansatz design, this approach can be extended to system sizes beyond the reach of classical simulation, enabling scalable training for larger quantum systems. This also enables a form of classical pre-training through gradient-based optimization prior to deployment on quantum hardware. The proposed approach is demonstrated on the Variational Quantum Eigensolver for obtaining the ground state of a spin model, showing that accurate results can be achieved with a scalable and computationally efficient procedure.

I. INTRODUCTION

Parametrized quantum circuits (PQCs) have attracted considerable attention in recent years due to their potential applications in Quantum Machine Learning (QML) and the growing availability of hardware capable of executing quantum algorithms for tasks of practical interest.

Despite the progress in hardware, a major challenge for QML remains the training time of these models. Evaluating and optimizing PQCs on quantum hardware is resource-intensive, with the added consideration that quantum devices are currently limited and experimental.

Obtaining gradients for PQC further exacerbates the problem. Computing analytical gradients via the parameter-shift [1] rule requires a number of circuit evaluations that scales with the number of parameters. For realistic tasks, such as generating a single MNIST image [2], the estimated time to perform a single training step can reach prohibitive times [3], making straightforward scaling unfeasible. Gradient-free optimizers, such as SPSA [4], COBYLA [5], and their variants, require a constant number of circuit evaluations per step and offer a partial workaround. However, these methods are often unstable in practice and do not fully alleviate the dependence on costly quantum hardware for training.

To mitigate these challenges, recent efforts have focused on designing gradient-efficient ansätze and formalizing tasks as through the evaluation of expectation values. In these approaches, the estimation of observables and their gradients can be classically simulable [6] or efficiently computed using a limited number of circuit evaluations [7], while the output remains classically hard to simulate. Examples include the Variational Quantum Eigensolver (VQE), which minimizes the expectation value of a Hamiltonian, and generative tasks whose goal can be formalized as matching the expectation values of randomly sampled Pauli strings in the Z basis to the corresponding values from the training set [8].

In this work, we propose a method to represent an observable as an explicit function of the circuit parameters in symbolic form, independent of any particular parameter assignment.

This approximate representation can be used to pre-train PQCs for the tasks described above, and subsequently fine-tuned via on-chip training or alternative optimization techniques.

In general, computing the exact functional representation of an observable is computationally challenging, as the number of terms grows (in the worst case scenario) exponentially with the number of parameters. To address this, we introduce two truncation schemes: a cutoff on the Pauli weight, which is particularly effective for locally scrambling ansätze [6], and a cutoff on the frequency, defined as the number of sine and cosine terms multiplied together in each product. These cutoffs enable an efficient approximation of the observable while keeping the computational complexity under control.

The paper is organized as follows. In Section II, we introduce the framework for the *propagation of observables* in quantum circuits. We begin in Section II A by describing the mechanism of exact propagation of observables in the Heisenberg picture.

Section II B examines the explicit representation of circuits and investigates how they might help in better understand the *barren-plateau* problem and in building better circuits.

Sections II C, II D, and II E provide the justification for the truncation schemes, which enable efficient propagation of observables at qubit numbers beyond classically simulable regimes.

Our results are presented in Section III, where we apply the method within the framework of the VQE in Section III A, using the Axial Next-Nearest Neighbor Ising (ANNI) model [9] as a test case. We justify the use of locally scrambling circuits for local spin models and

compare the propagated-energy estimates with exact diagonalization results.

Finally, in Section IV, we discuss other classes of problems to which this framework can be effectively applied and outline potential directions for improving the propagation method.

II. PROPAGATION OF OBSERVABLES

A. Exact propagation

In quantum computation, the Schrödinger representation is often used because it aligns intuitively with the circuit-based model, where the quantum state evolves as gates are applied. Given an initial state $|\psi\rangle$, the application of a unitary operator U transforms the state as

$$|\psi\rangle \rightarrow U|\psi\rangle. \quad (1)$$

An alternative perspective is offered by the *Heisenberg representation* [10], in which the evolution of observables is tracked instead of the quantum state. In this framework, the observable evolves *backwards* through the circuit via a similarity transformation,

$$O \rightarrow U^\dagger O U. \quad (2)$$

This backward evolution is referred to as *Pauli propagation* when restricted to the Pauli basis, since any observable can be expressed as a sum of Pauli operators.

During propagation, non-Clifford gates [11] induce a *branching effect*, where a single Pauli word (a tensor product of Pauli operators) evolves into a linear combination of two Pauli words. This branching causes the number of terms to grow exponentially with circuit depth. For instance, applying a rotation gate $R_Y(\theta)$ on the Pauli operator X results in

$$R_Y(\theta) X R_Y^\dagger(\theta) = \cos(\theta)X + \sin(\theta)Z, \quad (3)$$

where the original operator X branches into a combination of X and Z weighted by trigonometric functions of the parameter θ .

Unlike previous approaches such as [6] and [12], in this work the propagation is carried out *symbolically*, leaving the parameters $\vec{\theta}$ unassigned. Consequently, the final propagated observable is an analytic function of the circuit parameters.

Following the propagation through the similarity transformation in Eq. 2 and the matrix representation of the circuit's gates, two other key effects can be observed. First, two-qubit gates typically increase the *Pauli weight* of the propagated words, that is, the number of non-identity Pauli operators acting on different qubits. Second, each parametrized gate associated with a parameter θ_i multiplies the coefficient of the corresponding Pauli word by $\sin(\theta_i)$ or $\cos(\theta_i)$, while simultaneously branching it into two distinct terms, as seen in Eq. 3.

After the observable has been fully propagated through the circuit, it becomes a sum of Pauli words with parameter-dependent coefficients. To obtain its expectation value, we sandwich each Pauli word with the initial state, typically $|0\rangle^{\otimes n}$. During this step (referred to later as *trimming*), all Pauli words that contain any X or Y operators vanish, since their expectation value on $|0\rangle$ is zero. The remaining words, composed solely of Z and identity operators, each contribute their coefficients to the final expectation value.

An explicit example of an exact propagation is reported in Appendix A.

B. Explicit representation of circuits

Although the exact computation of all propagated terms for an observable does not scale efficiently and becomes computationally impractical even for modest circuit sizes due to branching, analyzing its representation at low depths and for a small number of qubits can still provide valuable insights. Such studies of the functional structure of observables may inform the design of more effective ansätze, potentially contributing to the development of *barren-plateau*-resistant architectures, as discussed later in this section.

For this study, we consider the 12-qubit local entangler ansatz, whose circuit representation is shown in Fig. 2 at depths 1, 2, 3, and 4, corresponding to successive iterations of the blocks inside the dashed rectangle. We focus on analyzing the propagation of the observable Z_0 through these circuit layers.

We define the *frequency* of a Pauli word as the number of sine and cosine factors it contains.

Fig. 1 shows the distribution of the final propagated terms in terms of Pauli weights (left) and frequencies (right), with each row corresponding to a different circuit depth. The colored terms (blue on the left, green on the right) represent the effective terms that survive the trimming process, contributing to the functional form of the observable, while the gray terms indicate those discarded during the expectation value computation.

The plots on the left illustrate how the Pauli weights increase with circuit depth. Specifically, at each iteration of the local entangler ansatz, any Pauli word can increase its weight by at most two, due to the two distinct layers of CNOT gates.

The plots on the right depict a gradual increase in the frequencies of the terms, with the maximum possible frequency equal to the total number of parameters. We observe an accumulation of higher frequency terms as the circuit depth grows.

The increase in the number of terms, the total number of parameters, and, most importantly the presence of higher frequencies may phenomenologically correlate with a reduced influence of individual parameters. This effect could help explain, in the context of expectation

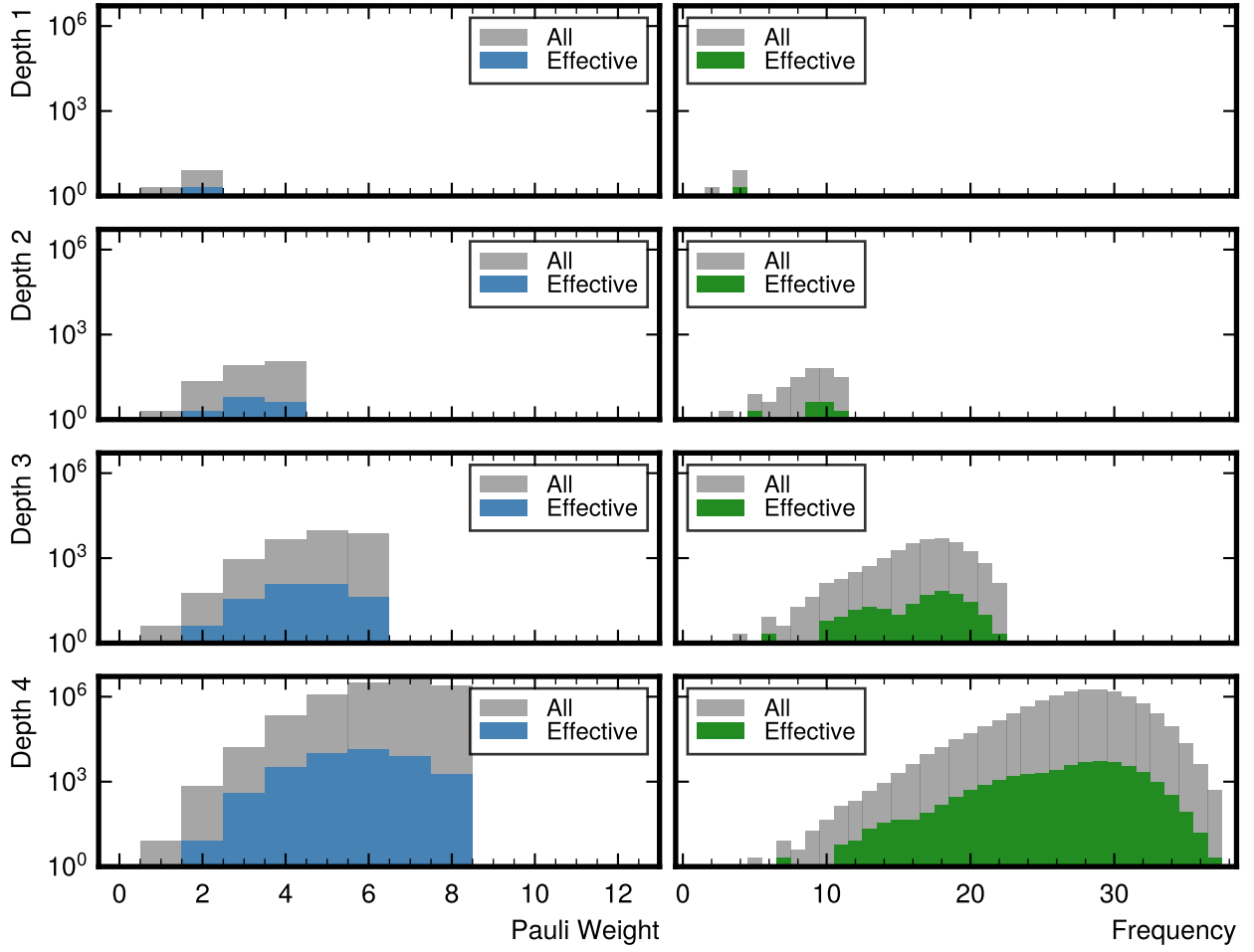


FIG. 1. Distribution of the Pauli weights (left) and frequencies (right) for the propagated observable Z_0 of the local entangler ansatz at different depths for 12 qubits.

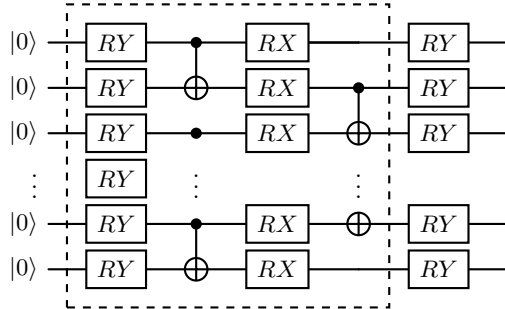


FIG. 2. Local entangler Ansatz

value estimation, the emergence of *barren-plateaus* during training.

Note that all the y-axes in the plots are displayed on a logarithmic scale, highlighting how rapidly the number of terms grows during propagation and illustrating why the exact method becomes computationally intractable, thus necessitating suitable cutoffs.

C. Truncation on Pauli Weight

During propagation, multi-qubit gates induce an increase in the weight of the propagated Pauli words. The work proposed in [6] showed that, on average, propagated observables from locally scrambling ansätze contain terms whose importance decreases exponentially with increasing weight. This property allows setting a cutoff value w_{cut} during propagation, discarding any words that exceed this cutoff and preventing them from further branching. This significantly reduces the computational burden.

D. Truncation on Frequencies

Other than the weights, additional terms during propagation can be reasonably discarded without significantly impacting the accuracy of the observables. During propagation, at each non-commuting parameterized gate acting on a Pauli word, that word branches and introduces either the sine or cosine of the corresponding parameter,

increasing the frequency. This results in words having coefficients that are products of sines and cosines of various elements of $\vec{\theta}$.

Since all sine and cosine values have absolute values less than or equal to 1, high-frequency words tend to contribute less on average because their coefficients are more likely to be close to zero. A more rigorous argument can be found in Appendix B.

Hence, by setting a cutoff value on the frequency, ν_{cut} , we can discard during propagation all those words whose frequency exceeds this threshold.

E. Error bound for joint truncations

In the two subsections above, we examined separately the effects of truncating the Pauli weights and the frequencies, showing how each approximation influences the accuracy of the propagated observables. Taken together, these results provide the intuition required to formulate an error bound for the *joint* truncation, in which both the maximal Pauli weight and the maximal frequency are truncated simultaneously.

Building on these arguments, one can reasonably assume that the total approximation error factorizes into independent contributions arising from weight truncation and frequency truncation.

Our symbolic propagation yields an exact objective $L(\boldsymbol{\theta}) = \langle \psi(\boldsymbol{\theta}) | O | \psi(\boldsymbol{\theta}) \rangle$ that can be written as a finite sum of Pauli words with trigonometric coefficients,

$$O(\boldsymbol{\theta}) = \sum_j c_j(\boldsymbol{\theta}) P_j, \quad (4)$$

where each Pauli word P_j has weight $w_j := \text{weight}(P_j)$ and each coefficient $c_j(\boldsymbol{\theta})$ is a product of sines and cosines of the circuit parameters. Truncating this expansion by discarding all terms with Pauli weight $w_j > w_{\text{cut}}$ or frequency $\nu_j > \nu_{\text{cut}}$ defines a truncated observable $O_{w_{\text{cut}}, \nu_{\text{cut}}}(\boldsymbol{\theta})$ and corresponding truncated loss $L_{w_{\text{cut}}, \nu_{\text{cut}}}(\boldsymbol{\theta})$.

To quantify the effect of this truncation, we assume a locality-induced decay of coefficients (formalized in Assumption 1 in App. B), that there exist constants $C_0 > 0$ and $0 < \alpha, \beta < 1$ such that

$$\sup_{\boldsymbol{\theta}} |c_j(\boldsymbol{\theta})| \leq C_0 \alpha^{w_j} \beta^{\nu_j}, \forall j. \quad (5)$$

This captures the heuristic that, for fixed-depth locally scrambling circuits on bounded degree architectures, high weight and high frequency terms are exponentially suppressed.

Combining this decay with an explicit combinatorial bound on the number of Pauli words of weight w and frequency- ν trigonometric monomials (App. B), we obtain the following uniform bound on the worst-case truncation error. Let

$$A := 3n\alpha, \quad B := 2P\beta, \quad (6)$$

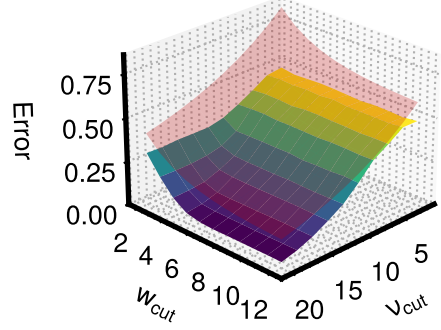


FIG. 3. Mean absolute errors at truncation values w_{cut} and ν_{cut} for uniformly sampled parameters of the Local Entangler Ansatz with 12 qubits and 3 repetitions of the unitary. The transparent red overlay represents the theoretical error bound obtained from Assumption 1.

where n is the number of qubits and P the number of trainable parameters. Provided $A < 1$ and $B < 1$ (i.e. the effective decay dominates the combinatorial growth), we show that

$$\sup_{\boldsymbol{\theta}} |L(\boldsymbol{\theta}) - L_{w_{\text{cut}}, \nu_{\text{cut}}}(\boldsymbol{\theta})| \leq C_0 \frac{(A^{w_{\text{cut}}+1} + B^{\nu_{\text{cut}}+1})}{(1-A)(1-B)}. \quad (7)$$

Hence the truncation error decays *exponentially* in both w_{cut} and ν_{cut} , up to a prefactor that depends only on (n, P) and the decay constants (C_0, α, β) . This makes precise the intuition that increasing the Pauli weight and frequency cutoffs yields rapidly diminishing error.

We obtain a similar control for the gradients. Let $\tilde{L}_{w_{\text{cut}}, \nu_{\text{cut}}}(\boldsymbol{\theta})$ denote the double truncated surrogate objective whose gradient is evaluated via the parameter-shift rule (see App. B 1 for the explicit Fourier representation). Under the same decay assumption on the Fourier coefficients, geometric tails in Pauli weight and frequency again control the contribution of discarded terms. In particular, for each parameter index j there exist constants $A_j, B_j > 0$ and $0 < \rho_w, \rho_\nu < 1$ such that

$$\sup_{\boldsymbol{\theta}} \left| \frac{\partial L}{\partial \theta_j}(\boldsymbol{\theta}) - \frac{\partial \tilde{L}_{w_{\text{cut}}, \nu_{\text{cut}}}}{\partial \theta_j}(\boldsymbol{\theta}) \right| \leq A_j \rho_w^{w_{\text{cut}}+1} + B_j \rho_\nu^{\nu_{\text{cut}}+1}. \quad (8)$$

Consequently, both the objective and its gradient converge uniformly as $w_{\text{cut}}, \nu_{\text{cut}} \rightarrow \infty$, and the parameter-shift gradients of the truncated surrogate provide a controllable approximation to the exact gradient landscape. Detailed derivations of Eqs. (7) and (8) are given in App. B and App. B 1.

To assess the validity of inequality (7), we evaluated the average absolute error for a range of cutoff values $(w_{\text{cut}}, \nu_{\text{cut}})$. For each pair, we uniformly sampled 10,000 parameter sets for the Local Entangler Ansatz with 12 qubits and 3 iterations of the unitary. Figure 3 reports the resulting mean absolute error for the observable

$$\sum_{i=1}^{12} Z_i.$$

As shown in the figure, the theoretical bound closely tracks the empirical error and exhibits the same exponential decay as w_{cut} and ν_{cut} increase. This agreement confirms the soundness of the underlying assumptions and demonstrates that accurate approximations can be achieved already at modest truncation values.

III. RESULTS

The ability to obtain a fast, approximate functional description of observables for a given circuit can be readily exploited in various QML algorithms that involve the minimization of a cost function dependent on one or more observables. Among these, the VQE [13] stands out as one of the most well-known examples, and an application of this approach is presented in the following subsection.

A. Variational Quantum Eigensolver

The VQE is a quantum algorithm designed to approximate the ground state of a given Hamiltonian H . For a parameterized quantum circuit $U(\boldsymbol{\theta})$, the variational state is defined as $|\psi(\boldsymbol{\theta})\rangle = U(\boldsymbol{\theta})|0\rangle$. The objective is to find the set of parameters $\boldsymbol{\theta}$ that minimizes the expectation value of the Hamiltonian, which corresponds to the energy

$$\mathcal{L}(\boldsymbol{\theta}) = \langle\psi(\boldsymbol{\theta})|H|\psi(\boldsymbol{\theta})\rangle, \quad (9)$$

such that the evolved state $|\psi(\boldsymbol{\theta})\rangle$ approximates the true ground state of H as closely as possible.

In this case, the observable to be propagated is the model's Hamiltonian itself, whose expectation value defines the loss function. The resulting variational state $|\psi(\boldsymbol{\theta})\rangle$ obtained after optimization can then be employed as an input to other QML models [14, 15], serving as a true quantum input data.

To illustrate an application of the symbolic propagation, the ANNNI model is used as an example, which Hamiltonian is defined as

$$H(\kappa, h) = -J \sum_{i=1}^N (X_i X_{i+1} - \kappa X_i X_{i+2} + h Z_i), \quad (10)$$

where J denotes the nearest-neighbor coupling constant (set to $J = 1$ without loss of generality), κ controls the strength of the next-nearest-neighbor interaction, and h represents the transverse magnetic field strength.

Depending on the values of κ and h , the system exhibits different phases arising from the competition between the transverse magnetic field and the two types of spin–spin interactions. Regardless of the specific parameter values, the Hamiltonian can be decomposed into

three distinct observables,

$$H(\kappa, h) = - \underbrace{\sum_{i=1}^N (X_i X_{i+1})}_{O_1} - \kappa \underbrace{\sum_{i=1}^N (X_i X_{i+2})}_{O_2} + h \underbrace{\sum_{i=1}^N (Z_i)}_{O_3}, \quad (11)$$

which only need to be propagated once. Consequently, a single propagation of these three observables is sufficient to obtain the expectation value of the Hamiltonian $H(\kappa, h)$ for any value of (κ, h) and any choice of parameters $\boldsymbol{\theta}$, for the given propagated circuit.

Once the explicit functional form of the Hamiltonian in terms of the parameters is obtained, the gradient of the loss function with respect to these parameters can be readily computed either analytically or via the *parameter-shift* rule [1], as both approaches yield the same gradient function.

A simulation was carried out on a system of 18 qubits with 4 iterations of the local entangler ansatz introduced in Fig. 2. The optimization was performed using the Adam optimizer [16] on the propagated observables, minimizing the expectation value of the observables defined in Eq. 11. While larger system sizes can, in principle, be treated with this method, we chose 18 qubits to allow direct comparison with exact statevector simulations, providing access to the true expectation values rather than their approximated counterparts. The results of these simulations are presented in Figs. 4–6.

Figures 4 and 5 correspond to simulations performed with cutoff values $w_{\text{cut}} = 8$ and $\nu_{\text{cut}} = 20$, respectively. Figure 4 presents a comparison between the ground-state energies of the ANNNI model obtained through exact diagonalization (left) and those computed via the VQE using the propagated Hamiltonian (right), while Fig. 5 reports the corresponding relative errors between the two results. Overall, the training achieves high accuracy with a limited yet scalable approach. The most significant deviations are observed in regions characterized by low values of h and high values of κ , corresponding to the so-called *antiphase* of the model, where the spin configuration exhibits a less regular and more non-local ordering pattern.

To further investigate the effect of the truncation parameters, Fig. 6 shows the training curves for a representative point of the phase diagram, $(\kappa, h) = (0.2, 0.4)$, obtained for various cutoff values of w_{cut} and ν_{cut} . Increasing w_{cut} leads to an immediate improvement in accuracy, with $w_{\text{cut}} = 8$ yielding results nearly indistinguishable from the exact values. A similar trend is observed for ν_{cut} , where a relatively small value of $\nu_{\text{cut}} = 20$ already provides near-perfect convergence, highlighting the efficiency and simulability of the proposed approximation.

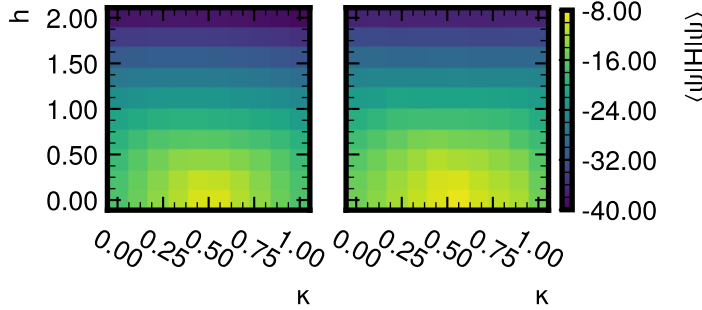


FIG. 4. Energies of the 18-spin ANNNI model at various values of κ and h , obtained using exact diagonalization (left) and by minimizing the function of the propagated Hamiltonian via gradient descent (right).

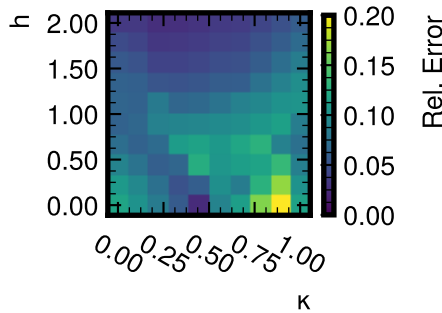
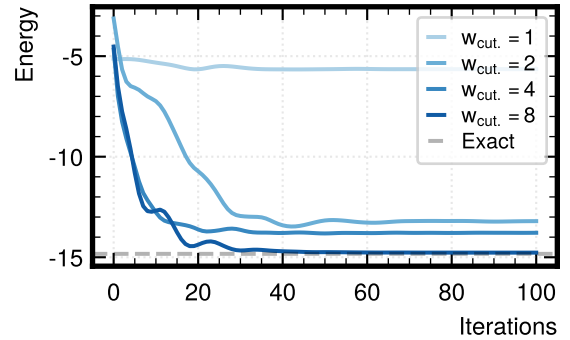


FIG. 5. Relative Errors of the energies between the diagonalized energies and the VQE energies from Fig. 4

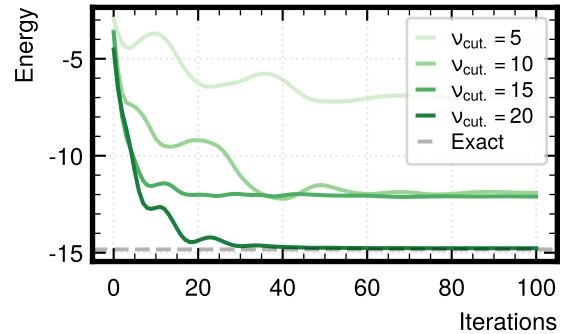
IV. DISCUSSIONS AND CONCLUSIONS

The VQE represents only one class of problems that can benefit from pre-training through the proposed propagation-based approach. Nevertheless, it remains a particularly promising example, as locally scrambling ansätze align naturally with the description of spin models, which, under most formulations, are governed by local interactions. Other QML tasks can similarly leverage this method, such as compression via anomaly-detection ansätze [15] and bitstrings generation through the formulation of the Maximum Mean Discrepancy (MMD) loss as randomly sampled observables in the Z basis [8]. However, in the latter case, the number of observables to be propagated can become prohibitively large, and the approximate training of the observable estimator may introduce excessive error, limiting the method's applicability.

This approach enables an effective form of off-chip pre-training, thereby alleviating the computational burden associated with costly on-chip quantum optimization. For such pre-training to be applicable, two main conditions must be satisfied: (i) the problem must be expressed through a loss function defined in terms of observables, and (ii) the chosen ansatz must exhibit favorable propagation properties, most notably, locally scrambling that



(a) VQE training with fixed $\nu_{\text{cut}} = 20$ and varying $w_{\text{cut}} \in \{1, 2, 4, 8\}$.



(b) VQE training with fixed $w_{\text{cut}} = 8$ and varying $\nu_{\text{cut}} \in \{5, 10, 15, 20\}$.

FIG. 6. Training curves of the Variational Quantum Eigensolver (VQE) applied to the ANNNI Hamiltonian at point $(\kappa, h) = (0.2, 0.4)$.

ensures efficient and accurate observable evaluations.

Future developments may focus on extending this framework along two main directions. First, the training procedure could be tested on circuits that are not classically simulable through direct wavefunction evolution, requiring suitable methods to verify the correctness of the obtained results. Second, the applicability of this approach could be broadened to other classes of QML problems beyond the VQE setting.

V. ACKNOWLEDGMENTS

This research was supported in part through the Maxwell computational resources operated at Deutsches Elektronen-Synchrotron DESY (Hamburg, Germany), a member of the Helmholtz Association HGF. ENGAGE has received funding from the European Union's Horizon 2020 Research and Innovation Programme under the Marie Skłodowska-Curie Grant Agreement No. 101034267.

VI. CODE AVAILABILITY

All code developed and used for the analyses presented in this work is publicly available on GitHub at <https://github.com/desyqml/Pauli-Propagator> [17].

[1] K. Mitarai, M. Negoro, M. Kitagawa, and K. Fujii, Quantum circuit learning, *Physical Review A* **98**, 10.1103/physreva.98.032309 (2018).

[2] L. Deng, The mnist database of handwritten digit images for machine learning research, *IEEE Signal Processing Magazine* **29**, 141 (2012).

[3] E. Recio-Armengol, S. Ahmed, and J. Bowles, Train on classical, deploy on quantum: scaling generative quantum machine learning to a thousand qubits (2025), arXiv:2503.02934 [quant-ph].

[4] J. C. Spall, An overview of the simultaneous perturbation method for efficient optimization, *Johns Hopkins apl technical digest* **19**, 482 (1998).

[5] M. J. Powell, A direct search optimization method that models the objective and constraint functions by linear interpolation, in *Advances in optimization and numerical analysis* (Springer, 1994) pp. 51–67.

[6] A. Angrisani, A. Schmidhuber, M. S. Rudolph, M. Cerezo, Z. Holmes, and H.-Y. Huang, Classically estimating observables of noiseless quantum circuits (2025), arXiv:2409.01706 [quant-ph].

[7] J. Bowles, D. Wierichs, and C.-Y. Park, Backpropagation scaling in parameterised quantum circuits, *Quantum* **9**, 1873 (2025).

[8] M. S. Rudolph, S. Lerch, S. Thanasilp, O. Kiss, O. Shaya, S. Vallecorsa, M. Grossi, and Z. Holmes, Trainability barriers and opportunities in quantum generative modeling, *npj Quantum Information* **10**, 10.1038/s41534-024-00902-0 (2024).

[9] W. Selke, The annni model—theoretical analysis and experimental application, *Physics Reports* **170**, 213 (1988).

[10] D. Gottesman, The heisenberg representation of quantum computers (1998), arXiv:quant-ph/9807006 [quant-ph].

[11] S. Bravyi and A. Kitaev, Universal quantum computation with ideal clifford gates and noisy ancillas, *Physical Review A* **71**, 10.1103/physreva.71.022316 (2005).

[12] Z.-L. Li and S.-X. Zhang, The dual role of low-weight pauli propagation: A flawed simulator but a powerful initializer for variational quantum algorithms (2025), arXiv:2508.06358 [quant-ph].

[13] J. Tilly, H. Chen, S. Cao, D. Picozzi, K. Setia, Y. Li, E. Grant, L. Wossnig, I. Rungger, G. H. Booth, *et al.*, The variational quantum eigensolver: a review of methods and best practices, *Physics Reports* **986**, 1 (2022).

[14] S. Monaco, O. Kiss, A. Mandarino, S. Vallecorsa, and M. Grossi, Quantum phase detection generalization from marginal quantum neural network models, *Physical Review B* **107**, 10.1103/physrevb.107.1081105 (2023).

[15] K. Kottmann, F. Metz, J. Fraxanet, and N. Baldelli, Variational quantum anomaly detection: Unsupervised mapping of phase diagrams on a physical quantum computer, *Physical Review Research* **3**, 10.1103/physrevresearch.3.043184 (2021).

[16] D. P. Kingma and J. Ba, Adam: A method for stochastic optimization (2017), arXiv:1412.6980 [cs.LG].

[17] S. Monaco, J. Slim, D. Krücker, and K. Borras, desyqml/pauli-propagator: Initial public release (2025).

[18] V. Bergholm, J. Izaac, M. Schuld, C. Gogolin, S. Ahmed, V. Ajith, M. S. Alam, G. Alonso-Linaje, B. Akash-Narayanan, A. Asadi, J. M. Arrazola, U. Azad, S. Banning, C. Blank, T. R. Bromley, B. A. Cordier, J. Ceroni, A. Delgado, O. D. Matteo, A. Dusko, T. Garg, D. Guala, A. Hayes, R. Hill, A. Ijaz, T. Isacsson, D. Ittah, S. Jhangiri, P. Jain, E. Jiang, A. Khandelwal, K. Kottmann, R. A. Lang, C. Lee, T. Loke, A. Lowe, K. McKiernan, J. J. Meyer, J. A. Montañez-Barrera, R. Moyard, Z. Niu, L. J. O’Riordan, S. Oud, A. Panigrahi, C.-Y. Park, D. Polatajko, N. Quesada, C. Roberts, N. Sá, I. Schoch, B. Shi, S. Shu, S. Sim, A. Singh, I. Strandberg, J. Soni, A. Száva, S. Thabet, R. A. Vargas-Hernández, T. Vincent, N. Vitucci, M. Weber, D. Wierichs, R. Wiersma, M. Willmann, V. Wong, S. Zhang, and N. Killoran, PennyLane: Automatic differentiation of hybrid quantum-classical computations (2022), arXiv:1811.04968 [quant-ph].

Appendix A: Step-by-step propagation

To illustrate how the Pauli propagation of observables works, we consider as an example the circuit shown in Fig. 7, focusing on the propagation of the observable Z_0 through the layers of the ansatz.

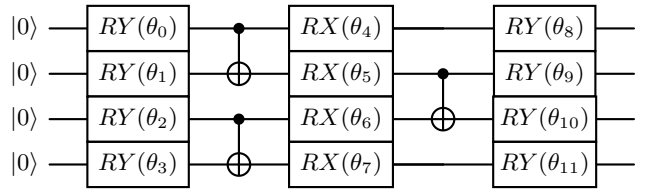


FIG. 7. Four-qubit local entangler ansatz with a single iteration (depth = 1).

- **Layer 5:** $(RY(\theta_8)_0 RY(\theta_9)_1 RY(\theta_{10})_2 RY(\theta_{11})_3)$

At this stage, the observable Z_0 is only affected by the gate $RY(\theta_8)_0$. According to the propagation rules in Table I, this evolves as:

$$Z_0 \rightarrow \cos \theta_8 Z_0 - \sin \theta_8 X_0 \quad (\text{A1})$$

- **Layer 4:** $(\text{CNOT}(1, 2))$

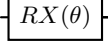
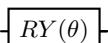
	$I \rightarrow I$ $X \rightarrow X$ $Y \rightarrow \cos \theta Y - \sin \theta Z$ $Z \rightarrow \cos \theta Z + \sin \theta Y$
	$I \rightarrow I$ $X \rightarrow \cos \theta X + \sin \theta Z$ $Y \rightarrow Y$ $Z \rightarrow \cos \theta Z - \sin \theta X$
	$I \otimes I \rightarrow I \otimes I$ $X \otimes I \rightarrow X \otimes X$ $Y \otimes I \rightarrow Y \otimes X$ $Z \otimes I \rightarrow Z \otimes I$ $I \otimes X \rightarrow I \otimes X$ $I \otimes Y \rightarrow Z \otimes Y$ $I \otimes Z \rightarrow Z \otimes Z$ $X \otimes X \rightarrow X \otimes I$ $Y \otimes X \rightarrow Y \otimes I$ $Z \otimes Y \rightarrow I \otimes Y$ $Z \otimes Z \rightarrow I \otimes Z$

TABLE I. Propagation rules for the $R_X(\theta)$, $R_Y(\theta)$, and CNOT gates.

Both terms of the observable commute with CNOT(1, 2), hence no transformation occurs:

$$\cos \theta_8 Z_0 - \sin \theta_8 X_0 \rightarrow \cos \theta_8 Z_0 - \sin \theta_8 X_0 \quad (\text{A2})$$

• **Layer 3:** $(RX(\theta_4)_0 \ RX(\theta_5)_1 \ RX(\theta_6)_2 \ RX(\theta_7)_3)$

Here only the gate $RX(\theta_4)_0$ affects the propagated observable. Using the propagation rules for $RX(\theta)$, we obtain:

$$\begin{aligned} \cos \theta_8 Z_0 - \sin \theta_8 X_0 &\rightarrow + \cos \theta_8 \cos \theta_4 Z_0 \\ &\quad + \cos \theta_8 \sin \theta_4 Y_0 \\ &\quad - \sin \theta_8 X_0 \end{aligned} \quad (\text{A3})$$

• **Layer 2:** $(\text{CNOT}(0, 1) \ \text{CNOT}(2, 3))$

The CNOT(0, 1) gate acts on all observables involving the first two qubits. Applying the propagation rules for the CNOT yields:

$$\begin{aligned} &+ \cos \theta_8 \cos \theta_4 Z_0 + \cos \theta_8 \sin \theta_4 Y_0 - \sin \theta_8 X_0 \\ &\downarrow \\ &+ \cos \theta_8 \cos \theta_4 Z_0 + \cos \theta_8 \sin \theta_4 Y_0 X_1 \\ &\quad - \sin \theta_8 X_0 X_1 \end{aligned} \quad (\text{A4})$$

• **Layer 1:** $(RY(\theta_0)_0 \ RY(\theta_1)_1 \ RY(\theta_2)_2 \ RY(\theta_3)_3)$

In this final layer, both $RY(\theta_0)_0$ and $RY(\theta_1)_1$ contribute to the evolution.

– **Action of $RY(\theta_1)_1$:**

$$\begin{aligned} &+ \cos \theta_8 \cos \theta_4 Z_0 + \cos \theta_8 \sin \theta_4 Y_0 X_1 \\ &- \sin \theta_8 X_0 X_1 \\ &\downarrow \\ &+ \cos \theta_8 \cos \theta_4 Z_0 \\ &+ \cos \theta_8 \sin \theta_4 \cos \theta_1 Y_0 X_1 - \cos \theta_8 \sin \theta_4 \sin \theta_1 Y_0 Z_1 \\ &- \sin \theta_8 \cos \theta_1 X_0 X_1 + \sin \theta_8 \sin \theta_1 X_0 Z_1 \end{aligned} \quad (\text{A5})$$

– **Action of $RY(\theta_0)_0$:**

$$\begin{aligned} &+ \cos \theta_8 \cos \theta_4 Z_0 \\ &+ \cos \theta_8 \sin \theta_4 \cos \theta_1 Y_0 X_1 - \cos \theta_8 \sin \theta_4 \sin \theta_1 Y_0 Z_1 \\ &- \sin \theta_8 \cos \theta_1 X_0 X_1 + \sin \theta_8 \sin \theta_1 X_0 Z_1 \\ &\downarrow \\ &+ \cos \theta_8 \cos \theta_4 \cos \theta_0 Z_0 - \cos \theta_8 \cos \theta_4 \sin \theta_0 X_0 \\ &+ \cos \theta_8 \sin \theta_4 \cos \theta_1 Y_0 X_1 - \cos \theta_8 \sin \theta_4 \sin \theta_1 Y_0 Z_1 \\ &- \sin \theta_8 \cos \theta_1 \cos \theta_0 X_0 X_1 - \sin \theta_8 \cos \theta_1 \sin \theta_0 Z_0 X_1 \\ &+ \sin \theta_8 \sin \theta_1 \cos \theta_0 X_0 Z_1 - \sin \theta_8 \sin \theta_1 \sin \theta_0 Z_0 Z_1 \end{aligned} \quad (\text{A6})$$

• **Expectation value computation (trimming):**

When computing the expectation value, each propagated observable is sandwiched between $\langle 0 |$ and $| 0 \rangle$. Only Pauli strings composed solely of Z or I operators survive this projection, leading to:

$$\langle Z_0 \rangle(\vec{\theta}) = - \sin \theta_8 \sin \theta_1 \sin \theta_0 + \cos \theta_8 \cos \theta_4 \cos \theta_0 \quad (\text{A7})$$

Appendix B: Contribution of High-Frequency Terms

When the training process reaches an optimal set of parameters $\{\theta_i\}$, the individual values of θ_i are typically correlated as a result of the optimization. However, the optimal configuration itself depends on the training data, which we may regard as random—especially in a stochastic learning procedure. Therefore, for the purpose of estimating the average contribution of high-frequency terms, it is reasonable to treat the parameters θ_i as random and independent.

For simplicity, we assume that the parameters are uniformly distributed, $\theta_i \sim U[0, 2\pi]$. Let $f_i(\theta_i)$ denote either $\sin \theta_i$ or $\cos \theta_i$. Under this assumption,

$$\mathbb{E}[f_i(\theta_i)] = 0, \quad \mathbb{E}[f_i^2(\theta_i)] = \frac{1}{2}.$$

For a product of ν such factors,

$$\mathbb{E}\left(\prod_{i=1}^{\nu} f_i^2(\theta_i)\right) = \prod_{i=1}^{\nu} \mathbb{E}[f_i^2(\theta_i)] = \frac{1}{2^{\nu}}.$$

This result shows that each additional sine or cosine factor contributes a fixed multiplicative reduction to the

overall variance. More generally, even for broader classes of distributions with zero mean and bounded support, the variance of the product decays exponentially with the number of factors ν . Hence, as the string of trigonometric functions grows longer, its expected value becomes increasingly concentrated around zero, justifying the truncation of high-frequency terms

ERROR BOUND FOR JOINT PAULI-WEIGHT AND FREQUENCY TRUNCATION

In Secs. II C and II D we introduced the truncation on Pauli weight w_{cut} and on frequency ν_{cut} . We now derive a simple, explicit upper bound on the error induced by this joint truncation.

Recall from Sec. II A that, after symbolic propagation and trimming on $|0\rangle^{\otimes n}$, any propagated observable $O(\vec{\theta})$ can be written as a finite sum of Pauli words with coefficients that are products of sines and cosines of the components of $\vec{\theta}$ as

$$O(\vec{\theta}) = \sum_j c_j(\vec{\theta}) P_j, \quad (\text{B1})$$

with

$$c_j(\vec{\theta}) = \prod_{\ell=1}^{\nu_j} f_{j,\ell}(\theta_{i_{j,\ell}}), \quad (\text{B2})$$

where each P_j is a Pauli word, ν_j is the frequency of that term (as defined in Sec. II B, i.e. the number of sine/cosine factors), and each $f_{j,\ell}$ is either sin or cos of one of the parameters. We write $w_j := \text{weight}(P_j)$ for the Pauli weight. Let $L(\vec{\theta}) = \langle \psi(\vec{\theta}) | O | \psi(\vec{\theta}) \rangle$ be the loss function, since $|\langle 0^{\otimes n} | P_j | 0^{\otimes n} \rangle| \leq 1, \forall P_j$, we can bound the total contribution of each term by

$$|c_j(\vec{\theta}) \langle 0^{\otimes n} | P_j | 0^{\otimes n} \rangle| \leq |c_j(\vec{\theta})|. \quad (\text{B3})$$

By-design, each factor satisfies $|f_{j,\ell}(\cdot)| \leq 1$, so that $|c_j(\vec{\theta})| \leq 1$ for all $\vec{\theta}$. This trivial uniform bound, however, does not control how the truncation error scales with w_{cut} and ν_{cut} . To obtain a meaningful scaling bound, we instead promote the locality and scrambling intuition to an explicit decay assumption on the coefficients.

Assumption 1 (Weight–frequency decay). *There exist constants $C_0 > 0$ and $0 < \alpha, \beta < 1$ such that, for any term j with Pauli weight w_j and frequency ν_j , its coefficient satisfies*

$$\sup_{\vec{\theta}} |c_j(\vec{\theta})| \leq C_0 \alpha^{w_j} \beta^{\nu_j}. \quad (\text{B4})$$

This captures the key idea that, for locally scrambling circuits at fixed depth and bounded-degree connectivity, large-weight and high-frequency terms appear only

through many small contributions and are exponentially suppressed on average.

Let $O_{w_{\text{cut}},\nu_{\text{cut}}}(\vec{\theta})$ denote the truncated observable obtained by discarding all terms with $w_j > w_{\text{cut}}$ or $\nu_j > \nu_{\text{cut}}$ during propagation, and let $L_{w_{\text{cut}},\nu_{\text{cut}}}(\vec{\theta})$ be the corresponding truncated loss. In the worst-case truncation error

$$\Delta_{w_{\text{cut}},\nu_{\text{cut}}}(\vec{\theta}) := L(\vec{\theta}) - L_{w_{\text{cut}},\nu_{\text{cut}}}(\vec{\theta}). \quad (\text{B5})$$

By construction, this difference is a sum over precisely those terms with $w_j > w_{\text{cut}}$ or $\nu_j > \nu_{\text{cut}}$.

We introduce the sets

$$\mathcal{J}_w := \{j : w_j > w_{\text{cut}}\}, \quad \mathcal{J}_\nu := \{j : \nu_j > \nu_{\text{cut}}\} \quad (\text{B6})$$

$$\mathcal{J}_{\text{cut}} := \mathcal{J}_w \cup \mathcal{J}_\nu \quad (\text{B7})$$

Using Eq. B3 and Assumption 1, we obtain

$$\begin{aligned} \sup_{\vec{\theta}} |\Delta_{w_{\text{cut}},\nu_{\text{cut}}}(\vec{\theta})| &\leq \sum_{j \in \mathcal{J}_{\text{cut}}} \sup_{\vec{\theta}} |c_j(\vec{\theta})| \\ &\leq \sum_{j \in \mathcal{J}_{\text{cut}}} C_0 \alpha^{w_j} \beta^{\nu_j}. \end{aligned} \quad (\text{B8})$$

To make this explicit, we bound how many terms can have given (w, ν) . For each weight w , the number of Pauli words on n qubits with $\text{wt}(P) = w$ is

$$N_w = \binom{n}{w} 3^w \leq (3n)^w. \quad (\text{B9})$$

For each frequency ν , the number of distinct products of ν sine or cosine factors over P parameters is at most $(2P)^\nu$ (there are P choices of parameter and two possible trigonometric functions for each factor), so we write

$$M_\nu \leq (2P)^\nu. \quad (\text{B10})$$

Thus, the total contribution from all terms with weight w and frequency ν is bounded by

$$C_0 \alpha^w \beta^\nu N_w M_\nu \leq C_0 (3n\alpha)^w (2P\beta)^\nu. \quad (\text{B11})$$

Summing over all discarded (w, ν) therefore yields

$$\sup_{\vec{\theta}} |\Delta_{w_{\text{cut}},\nu_{\text{cut}}}(\vec{\theta})| \leq \sum_{\substack{w, \nu: \\ w > w_{\text{cut}} \\ \text{or} \\ \nu > \nu_{\text{cut}}}} C_0 (3n\alpha)^w (2P\beta)^\nu. \quad (\text{B12})$$

Let $A := 3n\alpha$, and $B := 2P\beta$. Assuming that $A < 1$ and $B < 1$, which simply the encoding that the effective (weight, frequency) decay dominates the combinatorial

growth. We can then split the sum into a weight tail and a frequency tail as follows

$$\sup_{\vec{\theta}} |\Delta_{w_{\text{cut}}, \nu_{\text{cut}}}(\vec{\theta})| \leq C_0 \sum_{\substack{w, \nu: \\ w > w_{\text{cut}}}} A^w B^\nu + C_0 \sum_{\substack{w, \nu: \\ \nu > \nu_{\text{cut}}}} A^w B^\nu \\ =: \varepsilon_{\text{weight}}(w_{\text{cut}}) + \varepsilon_{\text{freq}}(\nu_{\text{cut}}). \quad (\text{B13})$$

Both $\varepsilon_{\text{weight}}$ and $\varepsilon_{\text{freq}}$ are geometric series. For the weight tail we have

$$\varepsilon_{\text{weight}}(w_{\text{cut}}) = C_0 \sum_{w=w_{\text{cut}}+1}^{\infty} \sum_{\nu=0}^{\infty} A^w B^\nu = C_0 \sum_{w=w_{\text{cut}}+1}^{\infty} A^w \sum_{\nu=0}^{\infty} B^\nu \\ = C_0 \left(\frac{1}{1-B} \right) \left(\frac{A^{w_{\text{cut}}+1}}{1-A} \right) \\ = \frac{C_0}{(1-A)(1-B)} A^{w_{\text{cut}}+1}. \quad (\text{B14})$$

Similarly, for the frequency tail,

$$\varepsilon_{\text{freq}}(\nu_{\text{cut}}) = C_0 \sum_{\nu=\nu_{\text{cut}}+1}^{\infty} \sum_{w=0}^{\infty} A^w B^\nu = C_0 \sum_{\nu=\nu_{\text{cut}}+1}^{\infty} B^\nu \sum_{w=0}^{\infty} A^w \\ = C_0 \left(\frac{1}{1-A} \right) \left(\frac{B^{\nu_{\text{cut}}+1}}{1-B} \right) \\ = \frac{C_0}{(1-A)(1-B)} B^{\nu_{\text{cut}}+1}. \quad (\text{B15})$$

Combining Eqs. B13, B14 and Eq. B15, we get at the final uniform bound

$$\sup_{\vec{\theta}} |L(\vec{\theta}) - L_{w_{\text{cut}}, \nu_{\text{cut}}}(\vec{\theta})| \leq \frac{C_0 (A^{w_{\text{cut}}+1} + B^{\nu_{\text{cut}}+1})}{(1-A)(1-B)} \quad (\text{B16})$$

In other words, under Assumption 1 the truncation error induced by the cutoffs w_{cut} and ν_{cut} decays *exponentially* in both cutoffs, up to a pre-factor that depends only on the system size and the decay constants. This makes precise the heuristic argument that increasing w_{cut} and ν_{cut} yields rapidly diminishing error.

1. Gradients under Pauli-weight and frequency truncation

The parameter-shift rule, when applied to the symbolically propagated observable, yields the same gradient of the truncated surrogate $\tilde{L}_{w_{\text{cut}}, \nu_{\text{cut}}}(\theta)$. For any gate set

admitting a valid parameter-shift rule. In general, however,

$$\nabla_{\theta} \tilde{L}_{w_{\text{cut}}, \nu_{\text{cut}}}(\theta) \neq \nabla_{\theta} L(\theta), \quad (\text{B17})$$

because the latter still contains contributions from Pauli words with $w(P) > w_{\text{cut}}$ or $\nu(P) > \nu_{\text{cut}}$. We now bound the difference between these two gradients.

Using the Fourier representation of $L(\theta)$ and its truncated version, as introduced above, the j -th component of the exact gradient can be written as

$$\frac{\partial L}{\partial \theta_j}(\theta) = \sum_{P,k} i k_j a_{P,k} e^{ik \cdot \theta}, \quad (\text{B18})$$

while for the truncated surrogate one obtains

$$\frac{\partial \tilde{L}_{w_{\text{cut}}, \nu_{\text{cut}}}}{\partial \theta_j}(\theta) = \sum_{\substack{P,k: \\ w(P) \leq w_{\text{cut}}, \\ \|k\|_1 \leq \nu_{\text{cut}}}} i k_j a_{P,k} e^{ik \cdot \theta}. \quad (\text{B19})$$

Their difference is therefore

$$\frac{\partial L}{\partial \theta_j}(\theta) - \frac{\partial \tilde{L}_{w_{\text{cut}}, \nu_{\text{cut}}}}{\partial \theta_j}(\theta) = \sum_{\substack{P,k: \\ w(P) > w_{\text{cut}} \\ \text{or} \\ \|k\|_1 > \nu_{\text{cut}}}} i k_j a_{P,k} e^{ik \cdot \theta}. \quad (\text{B20})$$

Taking the supremum over all θ and using $|e^{ik \cdot \theta}| = 1$ gives

$$\sup_{\theta} \left| \frac{\partial L}{\partial \theta_j}(\theta) - \frac{\partial \tilde{L}_{w_{\text{cut}}, \nu_{\text{cut}}}}{\partial \theta_j}(\theta) \right| \leq \sum_{\substack{P,k: \\ w(P) > w_{\text{cut}} \\ \text{or} \\ \|k\|_1 > \nu_{\text{cut}}}} |k_j| |a_{P,k}|. \quad (\text{B21})$$

Under the locality-induced decay of Fourier coefficients assumed in Sec. B, the right-hand side of Eq. B21 is dominated by convergent geometric tails in w_{cut} and ν_{cut} . Consequently, there exist constants $A_j, B_j > 0$ and $0 < \rho_w, \rho_\nu < 1$ such that

$$\sup_{\theta} \left| \frac{\partial L}{\partial \theta_j}(\theta) - \frac{\partial \tilde{L}_{w_{\text{cut}}, \nu_{\text{cut}}}}{\partial \theta_j}(\theta) \right| \leq A_j \rho_w^{w_{\text{cut}}+1} + B_j \rho_\nu^{\nu_{\text{cut}}+1}. \quad (\text{B22})$$

In particular, the gradient of the double-truncated surrogate converges uniformly to the gradient of the exact objective as $w_{\text{cut}}, \nu_{\text{cut}} \rightarrow \infty$, so that the parameter-shift rule provides a controllable approximation to $\nabla_{\theta} L$ via $\nabla_{\theta} \tilde{L}_{w_{\text{cut}}, \nu_{\text{cut}}}$.